Multiframe blind deconvolution of heavily blurred astronomical images

Yulia V. Zhulina

A multichannel blind deconvolution algorithm that incorporates the maximum-likelihood image restoration by several estimates of the differently blurred point-spread function (PSF) into the Ayers–Dainty iterative algorithm is proposed. The algorithm uses no restrictions on the image and the PSFs except for the assumption that they are positive. The algorithm employs no cost functions, input parameters, *a priori* probability distributions, or the analytically specified transfer functions. The iterative algorithm permits its application in the presence of different kinds of distortion. The work presents results of digital modeling and the results of processing real telescope data from several satellites. The proof of convergence of the algorithm to the positive estimates of object and the PSFs is given. The convergence of the Ayers–Dainty algorithm with a single processed frame is not obvious in the general case; therefore it is useful to have confidence in its convergence in a multiframe case. The dependence of convergence on the number of processed frames is discussed. Formulas for evaluating the quality of the algorithm performance on each iteration and the rule of stopping its work in accordance with this quality are proposed. A method of building the monotonically converging subsequence of the image estimates of all the images obtained in the iterative process is also proposed.

OCIS code: 100.0100.

1. Introduction

Image restoration has been widely studied in the literature because of its theoretical as well as practical importance in such fields as astronomy, medical imaging, and remote sensing. Its goal consists in recovering the original image from single or multiple blurred observations. Different restoration approaches depend on the particular degradation and image model assumed. Some types of image restoration algorithm assume that the point-spread function (PSF) is known *a priori* and attempt to invert it and reduce noise by using various amounts of information about the PSF, true image, and noise statistics. This is the task of the nonblind deconvolution. The single-channel nonblind 2D deconvolution has been studied extensively and techniques have been proposed for its solution.[1]

However, in many practical situations, the blur is partially known or unknown, because the exact knowledge about the mechanism of the image degradation process is not available. Therefore, the blind image restoration techniques have to be devised for restoration. The true image is assumed to be positive and to be composed of an object with known finite sizes against a uniformly gray background. This group is usually known as the iterative blind deconvolution method as proposed by Ayers and Dainty.[2] It is a famous pioneering work in blind deconvolution. A breakthrough in understanding blind deconvolution was the method of zero sheets proposed by Lane and Bates.[3] They have shown that any degraded image formed by convolving several individual components having compact support is automatically deconvolvable using zero sheet separation techniques provided their dimension is greater than one. Although conceptually the zero sheets are correct, they have little practical application since the algorithm is highly sensitive to noise.

Two-dimensional single-channel blind deconvolution has been investigated in Ref. 4. This method works on images that contain objects of finite support and have a uniform background. The area of the object support must be determined in advance. The only information required for restoration is the nonnegativity of the true image. The restoration procedure involves recursive inverse filtering of the blurred image to minimize a convex cost function. Extensions of this algorithm were proposed in Refs. 5 and 6. These

Y. V. Zhulina (yulia_julina@mtu-net.ru) is with the Vympel Interstate Joint Stock Corporation, Moscow 125319, Russia.

Received 28 November 2005; revised 10 April 2006; accepted 1 May 2006; posted 1 May 2006 (Doc. ID 66296).

0003-6935/06/287342-11$15.00/0

algorithms involve some regularization that assures various statistical properties of the image or constrains the estimated image and restoration filter according to some assumptions. This regularization is required to guarantee a unique solution and stability against noise and some model discrepancies.

The conjugate gradient method was proposed by Lane[7] to avoid the problems associated with the instability of the iterative blind deconvolution method. The procedure involves a minimization of some cost function by using the conjugate gradient optimization routine. In Ref. 8 a maximum-likelihood approach to blind deconvolution was presented. The authors incorporated *a priori* knowledge about object brightness distribution and the PSF described by phase aberrations in the pupil plane. In Ref. 9 the authors proposed a blind deconvolution algorithm that was rooted in the theory of generalized projections. They modified a pure-projection algorithm into one that permitted an incorporation of prior knowledge and had desirable convergence properties. This paper also reviews the deconvolution algorithm of Ref. 7 and analyzes some of the shortcomings caused by the penalty function it suggested.

If several differently blurred versions of one scene are available they can be used for enhancing the quality of the blind deconvolution algorithm. This task is named a multichannel (MC) blind deconvolution task. Typical examples of such multichannel measuring processes are remote sensing and astronomy, in which the same scene is observed at different time instants through a time-varying inhomogeneous medium such as the atmosphere. In case of multiple measurements, the restoration algorithm can exploit the redundancy present in the observations, and, in principle, it can achieve performance not obtainable from a single measure. Most of the available MC blind deconvolution methods can be grouped into classes based on their assumptions about the true image and the PSF or the assumptions regarding cost functions.

The first class of algorithms[10,11] identifies the PSF from the degraded image's characteristics before restoration of the image. A parametric model for the PSF is assumed with spectral nulls at locations dependent on specific parameter values; these parameter values are estimated by using the spectral nulls of the degraded image. The method is sensitive to noise and is limited to situations in which the PSF contains spectral nulls. In Refs. 12 and 13 another PSF restoration method is developed. The unknown distorted phases of the PSF are estimated by the maximum-likelihood method in an iterative process. The model of Gaussian noises is used in Ref. 12 and the model of Poisson noises is used in Ref. 13.

Another class of methods employs the constrained numerical optimization algorithms. The methodology described in Ref. 14 is one of constrained numerical optimization. It is a straightforward extension of the method proposed in Ref. 15 with modifications to accommodate real sensor artifacts such as noise, internal and external background, and nonuniform gain. Other methods of constrained optimization have been proposed,[8,16] and some have relied on essentially the same methodology as the one proposed in Ref. 15 with the differences being the method used for numerical optimization and the utilization of realistic sensor models. The work in Ref. 14 presents the application of a MC blind deconvolution method[15] to real telescope data.

In Ref. 17 the maximum-likelihood MC blind deconvolution together with a set of linear equality constraints is formulated quite generally, and it allows the same algorithm to handle a variety of different data collection schemes specified as data. Information about the data set is added to the algorithm in the form of linear equality constraints, which allows us to avoid writing a new algorithm for each type of data set. In Ref. 18 the blind deconvolution of a single blurred complex-valued image is considered. Images are contaminated with pseudorandom noise. The effect upon the algorithm's convergence of introducing various constraints is reported.

The problem of blind deconvolution appeared to be ill-posed with respect to both the image and the blur, and many regularization methods have been developed in the past ten years. The works using regularization can be considered as a special class of algorithms. One of the most successful regularization methods for denoising and deblurring is the total variation (TV) method.[19] TV has proved to be a good algorithm for edge-preserving denoising. The TV solution is associated with the highly nonlinear Euler–Lagrange equations, but several linearization schemes have been proposed to deal with this nonlinearity.[20–23] In Ref. 24, the 2D blurred images were built by using the linear motion blur and uniform blur, and a regularization approach was synthesized to join blur identification and image restoration. Certain types of regularization cost function work efficiently for some special types of images but are not suitable for general images (such as maximum entropy regularizations that produce sharp reconstructions of point objects, such as star fields in astronomical images.[25] The TV criterion penalizes the total amount of change in the image as the norm of the magnitude of its gradient. The most useful property of the TV criterion is that it tends to preserve the edges in the reconstruction,[19,25,26] as it does not severely penalize steep local gradients. The TV-based reconstruction algorithm has been proposed in Refs. 27 and 28, and its convergence has been verified in the case of the norm of the image gradient.

The next group of MC blind deconvolution algorithms represents an estimation of the blur functions directly by a simple one-step procedure and reduces the blind problem to the nonblind one if certain conditions are met. In Refs. 29 and 30 Harikumar and Bresler proposed a one-step subspace procedure that accomplishes blind restoration in a noise-free environment by finding a minimum eigenvector of a MC condition matrix. One disadvantage of the procedure is its vulnerability to noise. Reference 31 has proposed another MC method based on the greatest com-

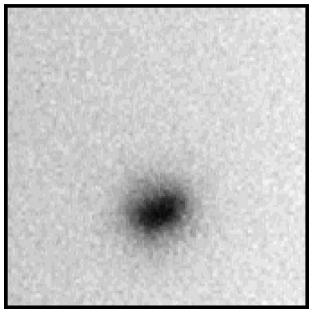

Fig. 1. Real image of the satellite Lacrosse-2.

mon divisor. A different MC approach proposed in Ref. 32 first constructs inverse far infrared filters and then estimates the original image by passing the degraded images through the inverse filters. Noise amplification also occurs here but can be attenuated to a certain extent by increasing the inverse filter order. In Ref. 32 it was shown that the blind blur identification algorithm is based on a relationship between outputs, which was also observed in Ref. 33 for 1D signals, and is derived in both the spatial and the frequency domains. In Ref. 34, a multichannel algorithm is proposed that incorporates the approach into the anisotropic denoising technique used in Refs. 29 and 30.

It is necessary to note that practically all the cited works restore the images in which main features are recognizable even in the blurred frames.[34] In Refs. 8 and 15 the binary star Capella is restored from strongly blurred data; however, very often we have the task of restoring more complex objects, for example, the images of satellites. A convincing example of real object restoration (the Hubble Space Telescope) with a simultaneous estimation of the phase aberrations is given in Ref. 14.

Almost all the cited works use one of the mathematical models of the blurs and synthesize the algorithm for this specific model. In reality, the data contain all the possible distortions simultaneously and the task does not obey any rigorous formulation.

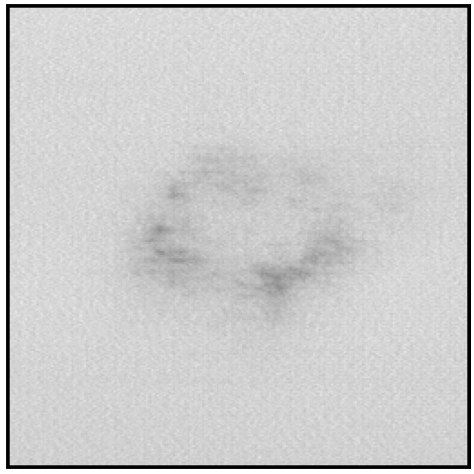

Fig. 3. Real image of the satellite Global Star.

In Figs. 1–4, real images of four different satellites obtained in the solar incoherent light by a telescope of the Science Industrial Corporation Astrophysika are shown. It is easy to see that they do not look like the photos of true space objects. Furthermore, not only the phase distortions but also the amplitude blurs of the field take place on the aperture of a telescope. Additional sources of distortion are the instrumentation errors of an optical receiver (nonlinear characteristics of a detector, pulse noises in the detector output, and others). The additive noises have to be classed with the distortions already mentioned (for example, the background field that takes place even in the absence of a space object). The Poisson noise of the optical receiver should be added to this background. Therefore the random background appears in all the figures.

In this paper I propose a MC blind deconvolution algorithm that incorporates the maximum-likelihood estimation of an object spectrum by several estimates of the independently blurred transfer functions into the Ayers–Dainty[2] iterative algorithm. The algorithm does not use *a priori* assumptions about the

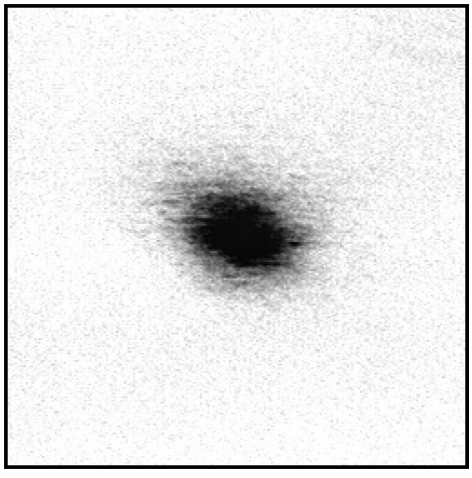

Fig. 2. Real image of the satellite Lacrosse-4.

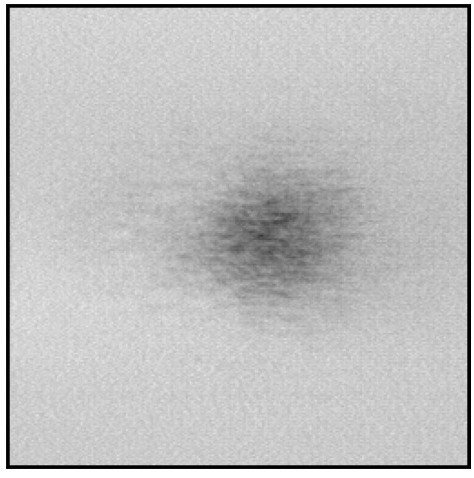

Fig. 4. Real image of the International Space Station.

object or the PSFs except for the assumption that they are positive. The algorithm does not employ any cost functions, input parameters, probability distributions, or the analytically specified transfer functions. It can be used in the presence of any types of distortion.

2. Task Statement

The task reported in Ref. 2 was as follows: there is a convolution function $O(\vec{r})$:

$$O(\vec{r}) = \int h(\vec{r} - \vec{r}_1)E(\vec{r}_1)\mathrm{d}^2\vec{r}_1 + n(\vec{r}),$$

in which $h(\vec{r})$ and $E(\vec{r})$ are unknown functions and are to be estimated, $n(\vec{r})$ is additive noise, $\vec{r}$ and $\vec{r}_1$ are vector coordinates of the point in 2D space. In Ref. 2 an iterative algorithm with restrictions on the functions $h(\vec{r})$ and $E(\vec{r})$ was proposed. The main restrictions on $h(\vec{r})$ and $E(\vec{r})$ are that both functions must be positive and unequal to zero in some area that is *a priori* defined. Reference 2 considers a case of a single-frame $O(\vec{r})$.

Now we consider a case in which there are M distorted frames. The unknown true image $E(\vec{r})$ is the same in all the frames. But we have

- M functions of convolution $O_m(\vec{r})(1 <= m <= M)$,
- M functions of their Fourier transform $C_m(\vec{\omega})$ $(1 <= m <= M)$, and
- M the unknown distorted impulse responses $h_m(\vec{r})(1 <= m <= M)$.

The restrictions on the image $E(\vec{r})$ and the impulse response $h_m(\vec{r})(1 <= m <= M)$ are the same: $E(\vec{r}) >= 0$ in all areas of the frame, $h_m(\vec{r}) >= 0$, $(1 <= m <= M)$. But we do not demand the advanced area of the object or the impulse response support. Further, we use the designation k for the number of the iteration cycle and $E^{(k)}(\vec{r})$ for the image estimate before imposing restrictions in this iteration. It can be presented as

$$E^{(k)}(\vec{r}) = E^{(+)(k)}(\vec{r}) - E^{(-)(k)}(\vec{r}), \tag{1}$$

where $E^{(+)(k)}(\vec{r})$ is the positive part of the estimate and $-E^{(-)(k)}(\vec{r})$ is the negative one. It is evident that these functions do not have any intersecting regions in their arguments $\vec{r}$. Respectively, the Fourier transform of the image estimate can be presented as

$$G^{(k)}(\vec{\omega}) = G^{(+)(k)}(\vec{\omega}) - G^{(-)(k)}(\vec{\omega}), \tag{2}$$

where $G^{(+)(k)}(\vec{\omega})$ is the Fourier transform of the positive part of the image and $G^{(-)(k)}(\vec{\omega})$ is the Fourier transform of the negative one taken with the opposite sign, and $\vec{\omega}$ is the coordinate in Fourier space.

As in Eq. (1), $h_m{}^{(k)}(\vec{r})$ is the designation for the PSF estimate with the number $m = (1, \ldots, M)$ within this iteration before imposing the restrictions. It also can be presented as

$$h_m{}^{(k)}(\vec{r}) = h_m{}^{(+)(k)}(\vec{r}) - h_m{}^{(-)(k)}(\vec{r}). \tag{3}$$

As in Eq. (2), the spectrum of the impulse response $h_m{}^{(k)}(\vec{r})$ with the number $(m = 1, \ldots, M)$ can be expressed through the sum of two spectra

$$H_m{}^{(k)}(\vec{\omega}) = H_m{}^{(+)(k)}(\vec{\omega}) - H_m{}^{(-)(k)}(\vec{\omega}), \tag{4}$$

where the first term on the right-hand side designates the spectrum of the positive part of the impulse response estimate, and the second term designates the spectrum of the negative one taken with the opposite sign. The algorithm begins with the number $k = 1$ and the initial approximation for $E^{(+)(k-1)}(\vec{r}) = E^{(+)(0)}(\vec{r})$, which is transformed by the Fourier transform as step 1. The result of the transform is function $G^{(+)(k-1)}(\vec{\omega}) = G^{(+)(0)}(\vec{\omega})$. Functions $H_m{}^{(k)}(\vec{\omega})$, $G^{(+)(k-1)}(\vec{\omega})$, and $C_m(\vec{\omega})$ are connected with relation

$$H_m{}^{(k)}(\vec{\omega})G^{(+)(k-1)}(\vec{\omega}) = C_m(\vec{\omega}). \tag{5}$$

Now all the spectra $H_m{}^{(k)}(\vec{\omega})(m = 1, \ldots, M)$ are calculated by dividing the right-hand side of Eq. (5) by spectrum $G^{(+)(k-1)}(\vec{\omega})$.

To decrease the instability of dividing when there are zeros in $G^{(+)(k-1)}(\vec{\omega})$, a small $\varepsilon^{(k)}$ should be added to the nominator when dividing. Then we arrive at step 2:

$$H_m{}^{(k)}(\vec{\omega}) = \frac{C_m(\vec{\omega})}{G^{(+)(k-1)}(\vec{\omega}) + \varepsilon^{(k)}}. \tag{6}$$

The question of choosing a value for $\varepsilon^{(k)}$ is discussed at the end of this section.

$H_m{}^{(k)}(\vec{\omega})$ is transformed by the inverse Fourier transform and the estimate $h_m{}^{(k)}(\vec{r})(m = 1, \ldots, M)$ is obtained as step 3. This estimate imposes restrictions and we get the estimate $h_m{}^{(+)(k)}(\vec{r})(m = 1, \ldots, M)$ as step 4. Now the Fourier transform of $h_m{}^{(+)(k)}(\vec{r})$ is performed and the spectrum $H_m{}^{(+)(k)}(\vec{\omega})(m = 1, \ldots, M)$ is obtained in step 5.

In the next step we have to estimate the Fourier transform of image $G^{(k)}(\vec{\omega})$. It can be obtained as the resolution of equation

$$\frac{\delta \ln\left[G^{(k)}(\cdot)\right]}{\delta G^{(k)}(\vec{\omega})} = 0, \tag{7}$$

where $\ln[G^{(k)}(\cdot)]$ is the likelihood function for $G^{(k)}(\vec{\omega})$:

$$\ln\left[G^{(k)}(\cdot)\right] = -\sum_{m=1}^{M}\int \left|H_m{}^{(+)(k)}(\vec{\omega})G^{(k)}(\vec{\omega}) - C_m(\vec{\omega})\right|^2 \times \mathrm{d}^2\vec{\omega}. \quad (8)$$

and $\dfrac{\delta \ln[G^{(k)}(\cdot)]}{\delta G^{(k)}(\vec{\omega})}$ is the functional derivative.

Resolving Eq. (8) for $G^{(k)}(\vec{\omega})$ we get

$$G^{(k)}(\vec{\omega}) = \sum_{m=1}^{M} \mu_m{}^{(k)}(\vec{\omega})C_m(\vec{\omega}), \quad (9)$$

where $\mu_m{}^{(k)}(\vec{\omega})$ is

$$\mu_m{}^{(k)}(\vec{\omega}) = \frac{H_m{}^{(+)(k)*}(\vec{\omega})}{\sum_{m=1}^{M}\left|H_m{}^{(+)(k)*}(\vec{\omega})\right|^2}. \quad (10)$$

A small value $\varepsilon_0{}^{(k)}$ should be added to the denominator in Eq. (10) to improve convergence:

$$\mu_m{}^{(k)}(\vec{\omega}) = \frac{H_m{}^{(+)(k)*}(\vec{\omega})}{\sum_{m=1}^{M}\left|H_m{}^{(+)(k)*}(\vec{\omega})\right|^2 + \varepsilon_0{}^{(k)}}. \quad (11)$$

We can omit the value $\varepsilon_0{}^{(k)}$ and use Eq. (10) in Eq. (9) if the number M is large enough. In this case the probability of zero in the numerator of Eq. (10) decreases.

As many repeated calculations have shown it is effective to use $\varepsilon_0{}^{(k)} = 0$ if

$$\mathrm{Num} = \underbrace{\min}_{\vec{\omega}}\left\{\sum_{m=1}^{M}\left|H_m{}^{(+)(k)*}\vec{\omega}\right|^2\right\} > 0$$

and to use as $\varepsilon_0{}^{(k)}$ the smallest above-zero value of $\sum_{m=1}^{M}|H_m{}^{(+)(k)*}(\vec{\omega})|^2$ if Num = 0. A similar principle can be used for the choice of $\varepsilon^{(k)}$ in Eq. (6), but it has to be applied to

$$\mathrm{Num}_E = \underbrace{\min}_{\vec{\omega}}\left\{\left|G^{(+)\{k-1\}}(\vec{\omega})\right|\right\}.$$

The calculation of Num and Num_E is performed over the discrete space of frequencies $\vec{\omega}$. The volume of the space is determined by the dimensions of the frame. All the operations in Eqs. (6)–(11) make up step 6. The inverse Fourier transform of Eq. (9) gives the $E^{(k)}(\vec{r})$ estimate (step 7). Then $E^{(k)}(\vec{r})$ imposes restrictions and we obtain a new estimate of the function $E^{(+)(k)}(\vec{r})$ (step 8). $E^{(+)(k)}(\vec{r})$ represents an initial approximation for the next iteration cycle. Now the number of iterations is increased to $k = k + 1$ and the entire process begins again.

An important question is how to make the correct initial approximation for the image estimate, i.e., function $E^{(+)(0)}(\vec{r})$. The principal demand is that one ought not to take the initial approximation for the image in the form of the delta function at $k = 1$, since this leads to a trivial solution and selection as the solution of the stagnant point of the algorithm (the image estimate remains to be delta function, the impulse response estimate remains to be the input frame). As repeated calculations of the model and real images have shown, the initial approximation for $E^{(+)(0)}(\vec{r})$ in a form of linear combination of the input frames gives the completely satisfactory results of convergence. In the results given in Section 4, the average of all the input frames was used as the initial approximation.

3. Method of Stopping the Algorithm

The Ayers–Dainty algorithm usually demonstrates the oscillating type of convergence. This can also be referred to as multiframe blind deconvolution. Therefore some error metric of the algorithm has to be defined and evaluated for each iteration. Many algorithms are synthesized on the basis of one or another error metric.[4,7,14,15,17,25–28] Among them, one powerful MC blind deconvolution algorithm is capable of working with different data collections.[17] The algorithm in Ref. 17 uses the maximum-likelihood estimation of the unknown phases on the pupil of the optical system. These phases are given parametrically in the form of a series with unknown coefficients. The error metric is introduced as a logarithm of the likelihood functional with added regularization parameters. Here I use the error metric as correlation of the true convolution function with the estimated convolution function on each iteration. This correlation is used only to determine the moment of stopping the algorithm but not for synthesis of it (the algorithm is given by the Ayers–Dainty scheme).

The error metric is calculated as follows:

(i) The convolution of the image estimate $E^{(+)(k)}(\vec{r})$ and the impulse response estimate $h_m{}^{(+)(k)}(\vec{r})(m = 1, \ldots, M)$ is calculated after each iteration with number k:

$$\hat{O}_m{}^{(k)}(\vec{r}) = \int h_m{}^{(+)(k)}(\vec{r} - \vec{r}_1) \times E^{(+)(k)}(\vec{r}_1)d^2\vec{r}_1 \quad (m = 1, \ldots, M). \quad (12)$$

(ii) The correlation function $Q_m{}^{(k)}(\vec{r})$ between $\hat{O}_m{}^{(k)}(\vec{r})$ and the input frame $O_m(\vec{r})$ is calculated as

$$Q_m{}^{(k)}(\vec{r}) = \int \hat{O}_m{}^{(k)}(\vec{r} + \vec{r}_1)O_m(\vec{r}_1)d^2\vec{r}_1 \quad (m = 1, \ldots, M). \quad (13)$$

(iii) Function $Q_m{}^{(k)}(\vec{r})$ is normalized to one by

$$Qn_m{}^{(k)}(\vec{r}) = \frac{Q_m{}^{(k)}(\vec{r})}{\sqrt{\int\left[\hat{O}_m{}^{(k)}(\vec{r}_1)\right]^2\mathrm{d}^2\vec{r}_1 \cdot \int[O_m(\vec{r}_1)]^2\mathrm{d}^2\vec{r}_1}} \quad (m = 1, \ldots, M). \quad (14)$$

(iv) The maximum of $Qn_m{}^{(k)}(\vec{r})$ over the coordinate space is calculated as

$$Qn\ \max_m{}^{(k)} = \max_{\vec{r}}\{Q_m{}^{(k)}(\vec{r})\}. \tag{15}$$

(v) $Qn\ \max_m{}^{(k)}$ is normalized to M:

$$Qn\ \max{}^{(k)} = \frac{1}{M}\sum_{m=1}^{M} Qn\ \max_m{}^{(k)}. \tag{16}$$

The value $Qn\ \max^{(k)}$ is used as an error metric of the algorithm performance. If $Qn\ \max^{(k)}$ increases in the iteration process, it means convergence of the algorithm. But it can also take place in the case of converging to a trivial solution (the image estimate tends to a delta function, the impulse response estimate tends to the input frame). This case never occurs at the beginning of the process. At first the algorithm finds a nontrivial solution but later it can disappear in the direction of the trivial solution. In this case the algorithm has to be stopped.

So we have three causes for stopping an algorithm: (a) the coefficient $Qn\ \max^{(k)}$ increases very slowly in the iteration process (stagnation of solution); (b) it tends to 1 but the image estimate tends to a trivial solution; and (c) the coefficient $Qn\ \max^{(k)}$ ceases to increase at all (the error metric oscillates and convergence does not come).

The error metric $Qn\ \max^{(k)}$ gives us the possibility of selecting the subset of the best images from the entire set of obtained images. Selecting the current image estimate with the maximum value of $Qn\ \max^{(k)}$ and recording it onto a disk, we obtain the set of images that monotonically converges to the best result (in the sense of $Qn\ \max^{(k)}$). The results shown in Section 4 are really from this set of best images.

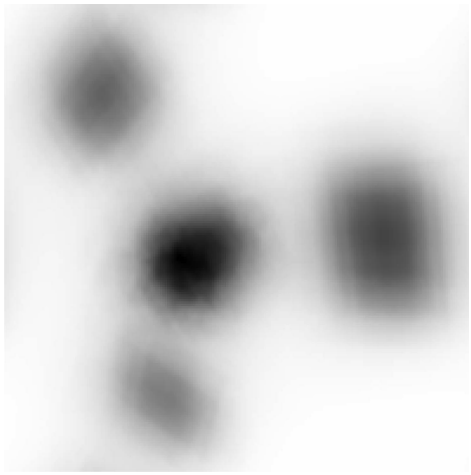

Fig. 5. Digitally modeled image of the satellite Ecco, frame 1.

Fig. 6. Digitally modeled image of the satellite Ecco, frame 2.

4. Results of Digital Modeling and Processing: Real Data

An image of the satellite Ecco has been taken from the Internet and convolved with the distorted impulse response of the system to build an example of digital modeling. The phase distortions were simulated independently in each frame. Two frames were processed ($M = 2$). The transfer function of the optical system was calculated by

$$H_m(\vec{\rho}) = \frac{1}{A}\int \Delta(\vec{r})e^{j\varphi_m(\vec{r})}\Delta(\vec{r}-\vec{\rho})e^{-j\varphi_m(\vec{r}-\vec{\rho})}\cdot \mathrm{d}^2\vec{r}. \tag{17}$$

Here A is a normalizing constant, and $\Delta(\vec{r})$ is the function of the aperture: it equals 1 inside the area of the objective lens and equals 0 outside it. $\varphi_m(\vec{r})$ is the function of phase distortions on the aperture in the frame with number m. It is possible to use some different statistical models to simulate $\varphi_m(\vec{r})$. In this example the Kolmogorov phase screens were used for simulation of phase distortions. These distortions are independent in the PSFs with different numbers

Fig. 7. Restoration of the satellite Ecco, 10th iteration.

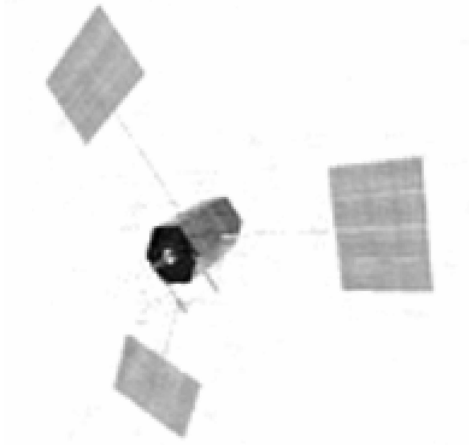

Fig. 8. Restoration of the satellite Ecco, 135th iteration.

$m(m = 1, \ldots, M)$. No additive noises were added to the image in the frames. Digital modeling shows the potential possibility of phase distortion compensation with the proposed algorithm.

Figures 5 and 6 represent the distorted frames in which restoration was made. Figure 7 is the result of the 10th iteration. Figure 8 shows the result of the 135th iteration. We can describe the change in the coefficient $Qn\ \max^{(k)}$ during the iteration process: On the 135th iteration $Qn\ \max^{(135)} = 0.9861$, on the 273rd iteration $Qn\ \max^{(273)} = 0.9913$, on the 608th iteration $Qn\ \max^{(608)} = 0.9914$. Between the 273rd and 608th iterations there were no other best-image estimates. So we can conclude that the algorithm has to be stopped after the 273rd iteration. Taking into account that the image estimates differ weakly on the 135th and 273rd iterations, the algorithm could, in fact, be stopped after the 135th iteration. It is necessary to admit that this refined digital modeling does not reflect such special features of real optical systems such as low resolution and severe distortion.

We next consider figures that represent the results of the algorithm performance in the case of real data. In Figs. 9 and 10, the restored image of the American radar imaging satellite Lacrosse-2 is presented. The restoration was made by 15 frames, one of which

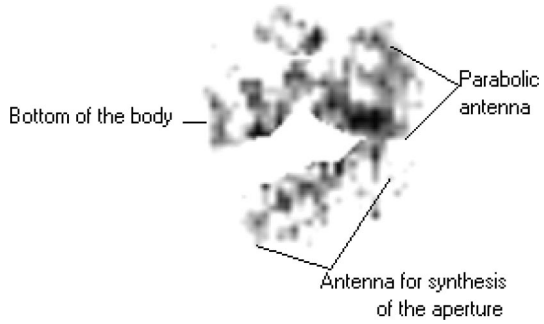

Fig. 10. Restoration of the satellite Lacrosse-2, 50th iteration, four times enlarged image.

is shown in Fig. 1. The sizes of the frames are 170 pixels × 170 pixels. Figure 9 shows the image enlarged two times and Figure 10 shows it enlarged four times. We can see four elements of the satellite construction: (i) an antenna for communications—a little cylinder at the top of the image from the left; (ii) the body of the satellite having the shape of a parallelepiped (under the cylinder); we see its bottom in this aspect; (iii) on the right of the body there is an antenna in the shape of a bowl. It is inclined approximately 15°–20° over the horizon, because we can see the black ellipse of the bowl. This antenna forms a transmitting signal; (iv) a long linear antenna is disposed under the antenna bowl. This linear antenna is designed for synthesis of the aperture in radar imaging. The satellite was disappearing from view at the moment of observation. The result was obtained after 50 iterations.

In Figs. 11 and 12, the restored image of another satellite of the same type, Lacrosse-4, is presented. The restoration was made by 11 frames, one of which is shown in Fig. 2. The sizes of the frames are 256 pixels × 256 pixels. Figure 11 shows the image enlarged twice, and Fig. 12 shows it enlarged four times. We can see the same four elements of this type

Fig. 9. Restoration of the satellite Lacrosse-2, 50th iteration, twice enlarged image.

Fig. 11. Restoration of the satellite Lacrosse-4, 59th iteration, twice enlarged image.

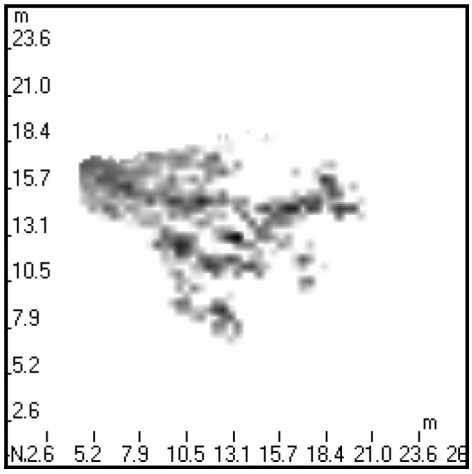

Fig. 12. Restoration of the satellite Lacrosse-4, 59th iteration, four times-enlarged image.

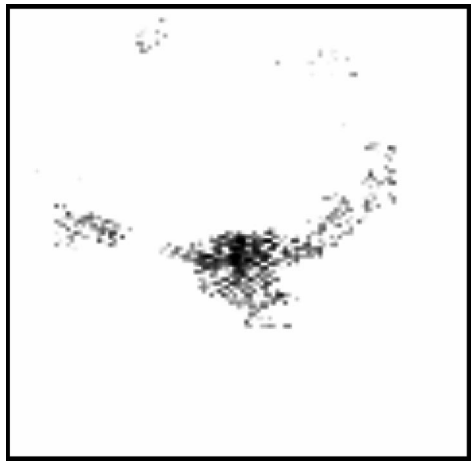

Fig. 14. Restoration of the satellite Global Star, 67th iteration, twice enlarged image.

of satellite: (i) an antenna for communications (a little cylinder at the top of the image but now from the right); (ii) the body of the satellite having the shape of a parallelepiped (at the background of the picture); (iii) the body ends with an antenna in the shape of a bowl, but in this case it has a polyhedral perimeter; (iv) a linear antenna for synthesis of the aperture is disposed under the antenna bowl. The satellite was moving toward the telescope at the moment of observation. The result was obtained after 59 iterations.

In Fig. 13 we see a scheme of the Lacrosse type of satellite from the Internet. There is a significant resemblance between Figs. 9–12 and Fig. 13. Everywhere there are parallelepiped shapes, a big round antenna, and a line antenna under it. The cylindrical antenna is in both Figs. 9 and 10 and Figs. 11 and 12. A restoration of both satellites permits us to conclude that the principles of the Lacrosse design are the same on the whole.

In Fig. 14 we see a restored image of the Global Star telephone communication satellite. Restoration was made by 11 frames, one of which is shown in Fig. 3. The twice enlarged image is shown in Fig. 14. The frame at Fig. 3 is 256 pixels $\times$ 256 pixels. After enlarging the frame a size of 512 pixels $\times$ 512 pixels was obtained, then it was cut off to the size of 256 pixels $\times$ 256 pixels. (The analogous operations were made to receive Figs. 10 and 12). The result in Fig. 14 was obtained after 67 iterations. The basic details of the object are visible in the restored image: (a) two large solar panels, (b) the body of the satellite is located between the panels, and (c) under the body one more panel of a smaller size is visible.

In Fig. 15, restoration of the International Space Station (ISS) was made. The telescope observed the station in October 2004, when the Shuttle spacecraft was attached to the ISS.

The restored image is enlarged two times in Fig. 15. The result was obtained after 159 iterations. The

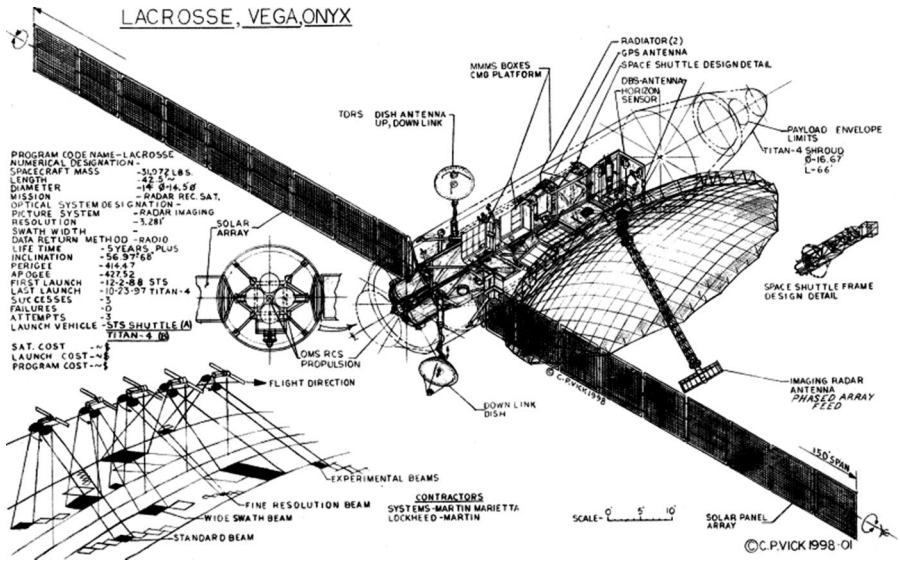

Fig. 13. Drawing of the Lacrosse satellite taken from the Internet.

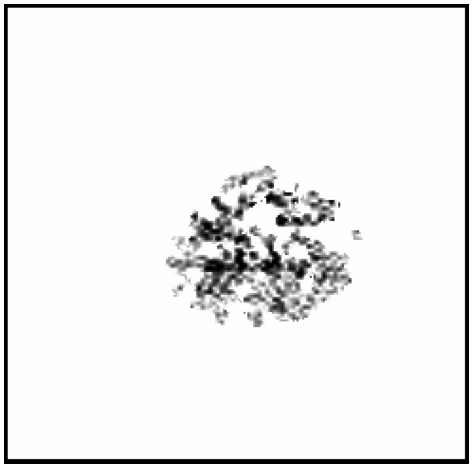

Fig. 15. Restoration of the ISS, 159th iteration, twice enlarged image.

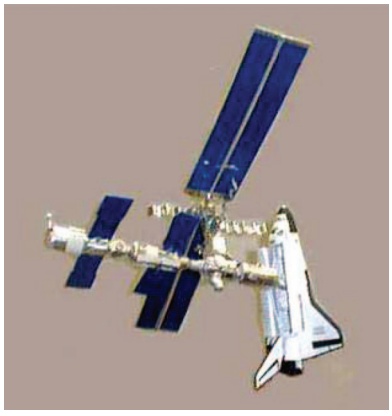

Fig. 16. (Color online) Picture of the ISS from the Internet.

resolution of the telescope was low so only the general contours of the ISS and the Shuttle are distinctly visible. However, it is clearly visible that the Shuttle was attached at two points (the nose and the body) almost as it is shown in the digital model of the ISS taken from the Internet (Fig. 16).

5. Conclusion

I have developed an algorithm for multichannel blind image restoration that combines the simplicity of the single-channel approach,[2] minimal *a priori* restrictions, the benefit of multichannel information, and does not use any cost functions with the exception for a choice of the best images. The algorithm does not demand any input parameters (noise level or order of blurs, for example) and deals only with the input blurred images. The main assumption is that the blurred PSFs in the different frames are independent.

The algorithm ensures convergence to the positive estimates of image and all PSFs. However, convergence to the positive estimates does not yet indicate the monotonic convergence to the true image. The algorithm demonstrates the oscillating type of convergence. Therefore the error metric for evaluating the quality of the algorithm performance and the rule of stopping algorithm in accordance with this quality are proposed. Also the rule of choice of the best subset of the restored images from the entire obtained set of images is proposed.

It is shown that the proposed algorithm gives satisfactory results for the restoration of real, heavily blurred images. The different distortions present in the processed images include the amplitude and phase distortions on the aperture of telescope and strong background in the optical receiver. Most of the works on image restoration deal with images in which the main features are recognizable. The proposed algorithm works with frames so strongly distorted that they cannot impart any idea about the shape of the object.

The multiframe algorithm permits us to obtain results much faster than the single-frame algorithm does. The processing of 10–15 real frames gives the result in the presence of strong additive noises not later than through 150–200 iterations with frame sizes of 256 pixels $\times$ 256 pixels. For comparison the single-frame Ayers–Dainty algorithm[2] obtains a result for the simulated speckle image without additive noise after 500 iterations with frame sizes of 64 pixels $\times$ 64 pixels.

The conjugate gradient method[8] obtains a result for the simulated and real speckle images of the binary stars after 3000 iterations with frame sizes of 128 pixels $\times$ 128 pixels. The plot of errors of the Ayers–Dainty algorithm that depends on the number of iterations is given in Ref. 7. It shows a considerable decrease in the error level after 2500 iterations with the frame of 32 pixels $\times$ 32 pixels. We have demonstrated the ability of the algorithm to recover images of 256 pixels $\times$ 256 pixels. The algorithm processed from 2 to 15 frames simultaneously during the various restorations. Satisfactory results can usually be obtained after approximately 100 iterations. The process takes approximately 80 min for 10 frames (256 pixels $\times$ 256 pixels) on a computer with 64 Mbytes of RAM and a clock rate of 400 MHz, approximately 45 min for 14 frames (256 pixels $\times$ 256 pixels) on a computer with 256 Mbytes of RAM and a clock rate of 1300 MHz, and approximately 15 min for 14 frames (256 pixels $\times$ 256 pixels) on a computer with 512 Mbytes of RAM and a clock rate of 3000 MHz.

It is important to note that there is no necessity to accelerate the calculations at the cost of the algorithms reliability (cutting the sizes of the frames, stopping an iterative process after a few iterations, for example) because the main problem of the blind deconvolution consists in the difficulties of the task, not in the capabilities of contemporary computers. It is necessary to admit that the restored images (Figs. 10–15) are not similar to the real photos of objects. It must be noted that these images are obtained from strongly distorted frames (Figs. 1–4). Furthermore, these images are obtained at distances of approximately 1000 km with a resolution worse than 1 m. It is not possible to obtain precise photos from such

distances even in the absence of atmosphere. However, we obviously obtain information about the elements of the objects construction: the body of a satellite (Figs. 9–12), its solar panels (Fig. 14), and its antennas (Figs. 9–12). It is interesting to note that the algorithm restores the polygonal structures in the satellites (the parallelepiped in a body in Figs. 9–12, the polyhedral perimeter of an antenna in Figs. 11 and 12, and the rectangular solar panels in Fig. 9), which means that the algorithm is capable of restoring the high space frequencies in the image. This fact was not observed in Refs. 2, 4, and 7–9. It is possible that the processing of several frames of large dimensions (256 pixels × 256 pixels and greater) provides more information with the maximum-likelihood estimate of the Fourier transform [see Eqs. (9) and (10)] than with other forms of algorithms.

In many cases precise information about the object is absent in the literature. Therefore it is interesting to reveal the presence of various elements in the image and to establish their position in the satellite. This is exactly the restoration of an unknown image.

Appendix A. Behavior of the Image and the PSF Spectrum Estimates in the Iterative Process

Here I investigate the quality of the estimates obtained by using the algorithm. All the designations have been introduced in Section 2. I also introduce the designations for partial estimates of the image spectrum $G_m^{(k)}(\vec{\omega})$ with each partial frame spectrum $C_m(\vec{\omega})$ $(m = 1, \ldots, M)$. This partial estimate $G_m^{(k)}(\vec{\omega})$ is connected with the functions $C_m(\vec{\omega})$ and $H_m^{(+)(k)}(\vec{\omega})$ [Eq. (4)] with the relation

$$G_m^{(k)}(\vec{\omega}) H_m^{(+)(k)}(\vec{\omega}) = C_m(\vec{\omega}). \tag{A1}$$

I also introduce the designations analogous to Eq. (2) for the partial estimates

$$G_m^{(k)}(\vec{\omega}) = G_m^{(+)(k)}(\vec{\omega}) - G_m^{(-)(k)}(\vec{\omega}), \tag{A2}$$

with the spectra of the positive and negative parts.

The partial estimates of the image in the coordinate space [the inverse Fourier transform of (A2)] are designated as $E_m^{(k)}(\vec{r})$ $(m = 1, \ldots, M)$.

From Eq. (5) we have

$$\left[H_m^{(+)(k)}(\vec{\omega}) - H_m^{(-)(k)}(\vec{\omega})\right] G^{(+)(k-1)}(\vec{\omega}) = C_m(\vec{\omega}). \tag{A3}$$

Equation (A1) is equivalent to

$$\left[G_m^{(+)(k)}(\vec{\omega}) - G_m^{(-)(k)}(\vec{\omega})\right] H_m^{(+)(k)}(\vec{\omega}) = C_m(\vec{\omega}). \tag{A4}$$

Equating Eq. (A3) to (A4) we obtain

$$\frac{G_m^{(k)}(\vec{\omega})}{G^{(+)(k-1)}(\vec{\omega})} + Q_m^{(k)}(\vec{\omega}) = 1 \quad (m = 1, \ldots, M), \tag{A5}$$

$$Q_m^{(k)}(\vec{\omega}) = \frac{H_m^{(-)(k)}(\vec{\omega})}{H_m^{(+)(k)}(\vec{\omega})}. \tag{A6}$$

Now I introduce the designations

$$\tilde{\mu}_m^{(k)}(\vec{\omega}) = \frac{\left|H_m^{(+)(k)}(\vec{\omega})\right|^2}{\sum_{m=1}^{M} \left|H_m^{(+)(k)}(\vec{\omega})\right|^2}, \tag{A7}$$

$$Q^{(k)}(\vec{\omega}) = \sum_{m=1}^{M} \tilde{\mu}_m^{(k)}(\vec{\omega}) Q_m^{(k)}(\vec{\omega}). \tag{A8}$$

Summarizing Eq. (A5) over all the frames with a multiplier $\tilde{\mu}_m^{(k)}(\vec{\omega})$, for Eqs. (A7) and (A8) I obtain

$$\frac{G^{(k)}(\vec{\omega})}{G^{(+)(k-1)}(\vec{\omega})} + Q^{(k)}(\vec{\omega}) = 1. \tag{A9}$$

In summation, we took into account Eqs. (9), (10), (A1), and (A7). I now analyze Eqs. (A5) and (A9). It is easy to see from Eq. (A5) that, if $Q_m^{(k)}(\vec{\omega})$ tends to zero (it means that the estimate of the PSF of number m tends to a positive function), then $G_m^{(k)}(\vec{\omega})/G^{(+)(k-1)}(\vec{\omega})$ tends to one for each $m = 1, \ldots, M$. [it means that the partial estimate of image $E_m^{(k)}(\vec{r})$ $(m = 1, \ldots, M)$ tends to a positive estimate of the whole algorithm $E^{(+)(k)}(\vec{r})$]. In contrast, if $Q_m^{(k)}(\vec{\omega})$ tends to one (the estimate of the PSF of number m diverges), then $G_m^{(k)}(\vec{\omega})/G^{(+)(k-1)}(\vec{\omega})$ tends to zero for each $m = 1, \ldots, M$. (The partial estimate of the image with number m also diverges.) So we observe the common tendency in the behavior of the estimates $h_m^{(k)}(\vec{r})$ and $E_m^{(k)}(\vec{r})$. Both of them converge or diverge simultaneously, but the partial estimates $E_m^{(k)}(\vec{r})$ $(m = 1, \ldots, M)$ are not the image estimates. The image spectrum estimate is defined by Eq. (9) and for this spectrum, Eq. (A9) is valid.

It is easy to see from Eq. (A9) that, if $Q^{(k)}(\vec{\omega})$ tends to zero (the weighted spectrum of the negative PSF estimates tends to zero), then $G^{(k)}(\vec{\omega})/G^{(+)(k-1)}(\vec{\omega})$ tends to 1. (The estimate of the image tends to a positive function.) On the other hand, if $Q^{(k)}(\vec{\omega})$ tends to 1, then $G^{(k)}(\vec{\omega})/G^{(+)(k-1)}(\vec{\omega})$ tends to zero. (The estimate of the image correspondingly diverges.) At first glance, the algorithm seems to show positive feedback, but it is not so actually since if we have a large enough M, then $Q^{(k)}(\vec{\omega})$ practically always tends to zero and convergence takes place. The weight $\tilde{\mu}_m^{(k)}(\vec{\omega})$ $(m = 1, \ldots, M)$, [Eq. (A7)] of the partial diverging estimate will be close to zero in the total sum. All the terms in the sum [Eq. (A8)] will be close to zero either because of the weight $\tilde{\mu}_m^{(k)}(\vec{\omega})$ or because of the value $Q_m^{(k)}(\vec{\omega})$ [Eq. (A6)] itself. As for the estimate of the image spectrum [Eq. (9)], the diverging partial estimate $G_m^{(k)}(\vec{\omega})$ will be excluded from Eq. (9) because of its small weight value $\tilde{\mu}_m^{(k)}(\vec{\omega})$. If at least one term remains in Eq. (9), the estimate of the image

will not diverge. It follows then that the greater the number M, the more reliable the algorithm performance.

Now we can give a qualitative estimate of the algorithm convergence in dependence on the number of M frames. Suppose that the probability of divergence of the one partial estimate equals P, and we designate the reliability of the algorithm as the probability of its convergence P_{conv}. To reach convergence we have to obtain at least a single converging partial estimate within each iteration, which means that the condition $P^M <= 1 - P_{\text{conv}}$ must be performed or

$$M >= \frac{\ln(1 - P_{\text{conv}})}{\ln \log P}, \tag{A11}$$

if $P = 0.5$ and $P_{\text{conv}} = 0.99$ then $M >= 7$; if $P = 0.9$ and $P_{\text{conv}} = 0.99$ then $M >= 44$. If we have a set of heavily distorted images the quantity of frames necessary for reliable performance of the algorithm could be a significant number.

The author thanks the Science Industrial Corporation Astrophysika for providing the telescope data. The author also thanks the anonymous reviewers for their comments and directions.

References

1. M. Banham and A. Katsaggelos, "Digital image restoration," IEEE Signal Process. Mag. **14,** 24–41 (1997).
2. G. R. Ayers and J. C. Dainty, "Iterative blind deconvolution method and its applications," Opt. Lett. **13,** 547–549 (1988).
3. R. Lane and R. Bates, "Automatic multichannel deconvolution," J. Opt. Soc. Am. A **4,** 180–188 (1987).
4. D. Kundur and D. Hatzinakos, "A novel blind deconvolution scheme for image restoration using recursive filtering," IEEE Trans. Signal Process. **46,** 375–390 (1998).
5. C. Ong and J. Chambers, "An enhanced NAS-RIF algorithm for blind image deconvolution," IEEE Trans. Image Process. **8,** 988–992 (1999).
6. M. Ng, R. Plemmons, and S. Qiao, "Regularization of RIF blind image deconvolution," IEEE Trans. Image Process. **9,** 1130–1138 (2000).
7. R. G. Lane, "Blind deconvolution of speckle images," J. Opt. Soc. Am. A **9,** 1508–1514 (1992).
8. E. Thiebaut and J. M. Conan, "Strict *a priori* constraints for maximum-likelihood blind deconvolution," J. Opt. Soc. Am. A **12,** 485–492 (March 1995).
9. Y. Yang, N. P. Galatsanos, and H. Stark, "Projection-based blind deconvolution," J. Opt. Soc. Am. A **11,** 2401–2409 (1994).
10. H. Pai and A. C. Bovik, "Exact multichannel blind image restoration," IEEE Signal Process. Lett. **4,** 217–220 (1997).
11. H. Pai and A. C. Bovik, "On eigenstructure-based direct multichannel blind image restoration", IEEE Trans. Image Process. **10,** 1434–1446 (2001).
12. P. A. Bakut and Y. V. Zhulina, "Measuring and compensating phase distortions in the images of short exposition," Opt. J. **65,** 5–61 (1998) (in Russian).
13. A. A. Kuriksha and Y. V. Zhulina, "Reconstruction of distorted optical images in the presence of Poisson signal fluctuations in the photoreceiver," J. Commun. Technol. Electron. **45,** 287–293 (2000).
14. T. J. Schulz, B. E. Stribling, and J. J. Miller, "Multiframe blind deconvolution with real data: imagery of the Hubble Space Telescope," Opt. Express **1,** 355–362 (1997).
15. T. J. Schulz, "Multiframe blind deconvolution of astronomical images," J. Opt. Soc. Am. A **10,** 1064–1073 (1993).
16. S. M. Jefferies and J. C. Christou, "Restoration of astronomical images by iterative blind deconvolution," Astrophys. J. **63,** 862–874 (1993).
17. M. G. Lofdahl, "Multi-frame blind deconvolution with linear equality constraints," in *Image Reconstruction from Incomplete Data II,* P. J. Bones, M. A. Fiddy and R. P. Millane, eds., Proc. SPIE **4792,** 146–155 (2002).
18. B. L. K. Davey, R. G. Lane, and R. H. T. Bates, "Blind deconvolution of noisy complex-valued image," Opt. Commun. **69,** 353–356 (1989).
19. L. Rudin, S. Osher, and E. Fatemi, "Nonlinear total variation based noise removal algorithms," Physica D **60,** 259–268 (1992).
20. C. Vogel and M. Oman, "Iterative methods for total variation denoising," SIAM (Soc. Ind. Appl. Math.) J. Sci. Comput. **17,** 227–238 (1996).
21. C. Vogel and M. Oman, "Fast, robust total variation-based reconstruction of noisy, blurred images," IEEE Trans. Image Process. **7,** 813–824 (1998).
22. T. Chan, G. Golub, and P. Mulet, "A nonlinear primal-dual method for total variation-based image restoration," SIAM (Soc. Ind. Appl. Math.) J. Sci. Comput. **20,** 1964–1977 (1999).
23. D. Geman and G. Reynolds, "Constrained restoration and the recovery of discontinuities," IEEE Trans. Pattern Anal. Mach. Intell. **14,** 367–383 (1992).
24. Y.-L. You and M. Kaveh, "A regularization approach to joint blur identification and image restoration," IEEE Trans. Image Process. **5,** 416–28 (1996).
25. A. Bovik, Handbook of Image and Video Processing (Academic, 2000).
26. T. F. Chan, S. Osher, and J. Shen, "The digital TV filter and nonlinear denoising," IEEE Trans. Image Process. **10,** 231–241 (2001).
27. T. Chan and C. Wong, "Total variation blind deconvolution," IEEE Trans. Image Process. **7,** 370–375 (1998).
28. T. F. Chan and C. K. Wong, "Convergence of the alternating minimization algorithm for blind deconvolution," Linear Algebr. Appl. **316,** 259–285 (2000).
29. G. Harikumar and Y. Bresler, "Perfect blind restoration of images blurred by multiple filters: Theory and efficient algorithms," IEEE Trans. Image Process. **8,** 202–219 (1999).
30. G. Harikumar and Y. Bresler, "Efficient algorithms for the blind recovery of images blurred by multiple filters," in Proceedings of IEEE International Conference on Image Processing (IEEE, 1996), Vol. 3, pp. 97–100.
31. S. Pillai and B. Liang, "Blind image deconvolution using a robust GCD approach," IEEE Trans. Image Process. **8,** 295–301 (1999).
32. G. Giannakis and R. Heath, "Blind identification of multichannel FIR blurs and perfect image restoration," IEEE Trans. Image Process. **9,** 1877–1896 (2000).
33. G. Xu, H. Liu, L. Tong, and T. Kailath, "A least-squares approach to blind channel identification," IEEE Trans. Signal Process. **43,** 2983–2993 (1995).
34. F. Sroubek and J. Flusser, "Multichannel blind iterative image restoration," IEEE Trans. Image Process. **12,** 1094–1106 (2003).